

Miniature Magnetic Resonance Imaging System for *in situ* Monitoring of Bacterial Growth and Biofilm Formation

Qi Zhou ¹, Graduate Student Member, IEEE, Shuhao Fan ², Graduate Student Member, IEEE, Ka-Meng Lei ¹, Senior Member, IEEE, Donhee Ham ³, Fellow, IEEE, Rui P. Martins ⁴, Life Fellow, IEEE, and Pui-In Mak ¹, Fellow, IEEE

Abstract—*In situ* monitoring of bacterial growth can greatly benefit human healthcare, biomedical research, and hygiene management. Magnetic resonance imaging (MRI) offers two key advantages in tracking bacterial growth: non-invasive monitoring through opaque sample containers and no need for sample pretreatment such as labeling. However, the large size and high cost of conventional MRI systems are the roadblocks for *in situ* monitoring. Here, we proposed a small, portable MRI system by combining a small permanent magnet and an integrated radio-frequency (RF) electronic chip that excites and reads out nuclear spin motions in a sample, and utilize this small MRI platform for *in situ* imaging of bacterial growth and biofilm formation. We demonstrate that MRI images taken by the miniature—and thus broadly deployable for *in situ* work—MRI system provide information on the spatial distribution of bacterial density, and a sequential set of MRI images taken at different times inform the temporal change of the spatial map of bacterial density, showing bacterial growth.

Index Terms—Bacterial growth, biofilm, *in situ* monitoring, miniaturized MRI.

I. INTRODUCTION

THE ability to monitor bacterial growth and colony formation *in situ* holds significant importance in human healthcare, hygiene management, ecological engineering, water treatment, and biotechnology. For example, tracking bacterial

aggregation in wounds and infusion tubes can help manage infection in postoperative patients [1]; evaluating bacterial development in groundwater or soil contaminants is beneficial for studying the effectiveness of biodegradation [2]; surveilling biofilm formation within water pipe networks may contribute to control biofouling and biocorrosion [3]; and analyzing the distribution of microorganism communities within microbial fuel cell can offer strategies to improve productivity [4]. In light of their importance, an extensive range of biosensors for bacterial monitoring has been developed [5]. Optical biosensors combined with fluorescent nucleic acid stains [6], [7], surface plasmon resonance [8], [9], or chemical luminescence [10], [11] can produce high-resolution images of bacterial distribution with remarkable specificity. Moreover, direct and indirect electrochemical biosensors [12] enable the determination of bacterial concentrations through property changes of medium or electrode surfaces, such as impedance [13], capacitance [14], [15], amperometry [16], and conductivity [17], [18], [19].

Nuclear magnetic resonance (NMR) offers a non-invasive and non-destructive pathway for sensing bacterial presence. Non-zero spin nuclei such as ¹H, ¹³C, and ¹⁹F pose a magnetic moment. When positioned in an external magnetic field and subject to additional magnetic fields, they yield an NMR signal that provides molecular-level insights. During bacterial growth, the presence of bacteria can alter the transverse relaxation time (T_2)—the characteristic decay time of the transverse magnetization of a collection of proton spins—of the NMR signal [20]. Hence, we can exploit the NMR to assess the bacterial growth. In addition, bacterial accumulation that adds a biopolymer gel-like phase to the pore walls and biomacromolecules to the fluid restricts the diffusion of the molecules and affects the NMR relaxation signal [21]. Vogt et al. [22] proposed distinguishing growing biofilms from porous media through intensified T_2 -relaxation due to the molecular exchange between the protons from biofilm and bulk water. These discoveries have paved the way for various applications in monitoring bacterial growth process. For instance, Kirkland et al. [23] detected the biogeochemical activity of contaminants in a lab-scale bioreactor, while Zhang et al. [24] characterized biofilm development process. Detection of biofouling in natural sand media [25] and subsurface biofilm [26] using a low-field NMR platform demonstrated the potential for on-site monitoring of the growth and decay of biofouling.

Manuscript received 6 November 2023; revised 18 January 2024; accepted 20 February 2024. Date of publication 23 February 2024; date of current version 27 September 2024. This work was supported in part by the Macao Science and Technology Development (FDCT) under Grant 004/2023/SKL, Grant 0071/2020/A2, and Grant 0149/2022/A3, and in part by the University of Macau Research Committee (MYRG2020-00132-IME). This paper was recommended by Associate Editor P. Motto Ros. (Corresponding author: Ka-Meng Lei.)

Qi Zhou, Shuhao Fan, Ka-Meng Lei, and Pui-In Mak are with the State Key Laboratory of Analog and Mixed-Signal VLSI/Institute of Microelectronics, University of Macau, Macao 999078, China, and also with the Department of ECE/Faculty of Science and Technology, University of Macau, Macao 999078, China (e-mail: kamenglei@um.edu.mo).

Donhee Ham is with the Harvard John A. Paulson School of Engineering and Applied Sciences, Harvard University, Cambridge, MA 02138 USA.

Rui P. Martins is with the State Key Laboratory of Analog and Mixed-Signal VLSI/Institute of Microelectronics, University of Macau, Macao 999078, China, and also with the Department of ECE/Faculty of Science and Technology, University of Macau, Macao 999078, China, on leave from the Instituto Superior Técnico, Universidade de Lisboa, 1649-004 Lisbon, Portugal.

Digital Object Identifier 10.1109/TBCAS.2024.3369389

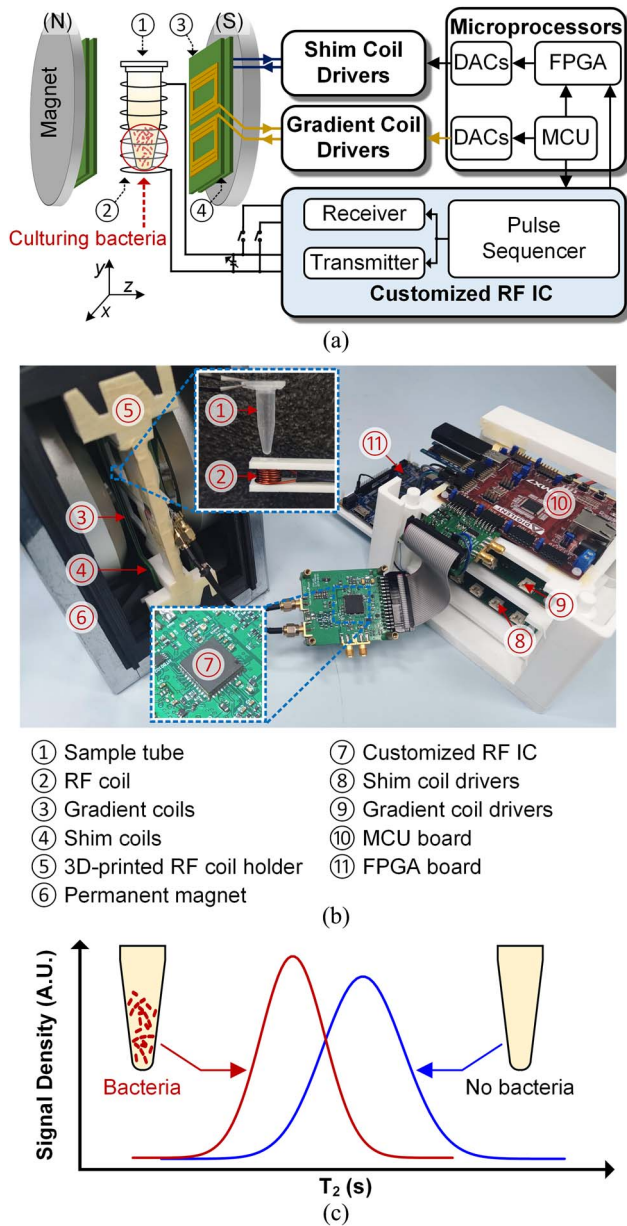


Fig. 1. (a) The miniaturized MRI system combines a permanent magnet, a customized RF IC, and a system of RF, gradient, and shim coils. (b) The experimental setup of the miniature MRI system. For clarity, coil drivers are disconnected from the coils in the picture. The compact footprint allows for placing the entire setup in different apparatuses (e.g., inside a temperature or gas chamber) to broaden the culturing scenario. (c) The simplified principle of using NMR/MRI to monitor bacterial growth by observing the reduction in T_2 due to bacterial accumulation.

Magnetic resonance imaging (MRI), derived from NMR with additional spatial encoding field gradients, enables additional imaging capabilities of the object under screening within opaque sample-containing tubes or pipes without the need for sample pretreatment (e.g., labeling). MRI could thus serve as an attractive alternative for mapping bacterial growth. Efforts have been made to track bacterial growth or presence using commercial MRI equipment: Seymour et al. [27] used MRI to non-invasively measure the pore scale dynamics and biofilm accumulation in a homogeneous model porous media through

velocity imaging and magnetic relaxation weighted imaging, and Caizán-Juanarena et al. [28] visualized biofilm distribution and volume increase process on active carbon granular anodes using MRI, aiming to improve the efficiency of microbial fuel cells for wastewater treatment.

Conventional MRI systems designed for medical imaging purposes are equipped with superconducting magnets and discrete radioactive-frequency (RF) electronics, rendering them bulky and expensive for broad deployment for *in situ* work. Recent advancements [29], [30] in integrated circuits (IC) technology have led to the development of miniaturized NMR [31], [32], [33], [34] and MRI systems [35], [36], [37]. Together with substituting the power-/resource-depleting superconducting magnet by a permanent magnet [38], [39], [40], [41], they significantly reduce the footprint and cost of the MRI equipment, making them more accessible for *in-situ* applications [42], [43].

Here, we demonstrate *in situ* monitoring of bacterial growth and biofilm formation using a small, portable ^1H MRI system with a permanent magnet and customized IC [Fig. 1(a) and 1(b)]. It primarily includes a permanent magnet that allows for unhampered growth environments for bacteria, including temperature conditions, a customized IC that excites the protons inside the samples and captures their signals in a compact footprint to enable on-site monitoring, and peripheral circuits for generating the magnetic field gradients to spatially encode the signals from the protons. The system acquires T_2 (or R_2) map of culturing bacteria from the T_2 -weighted images (T2WI) [Fig. 1(c)]. The proposed method does not require special sample pretreatment, transparency of the sample container, or cleanliness of sensitive elements, making it handy and feasible for *in situ* applications. In addition, in this work, we addressed the impact of magnetic field drift on the image quality due to the deployment of the permanent magnet and innovated a software-domain calibration method to tackle such limitations, enhancing the practicality of the proposed system under different conditions.

II. METHODOLOGY

A. Electronics for Miniaturized MRI System

The compact, portable MRI system is schematically illustrated in Fig. 1(a). Its backbone consists of a NdFeB permanent magnet (NMR14030-037, DEXINMAG, China) with a static magnetic field (B_0) of 0.37 T (the corresponding NMR Larmor frequency, f_L , for ^1H proton spins is approximately 15.7 MHz) and a customized RF IC [44]. The RF chip, in conjunction with a solenoidal RF coil surrounding a sample, is used to excite ^1H proton spins of the sample by transmitting the RF magnetic field and to detect the NMR signal induced in the RF coil by spin precessions, both at frequencies at or around f_L . The system also contains 5 pairs of shim coils to lessen the inhomogeneity of the static field B_0 of the permanent magnet. In addition, for imaging, the system features 3 pairs of gradient coils to introduce field gradients—on top of the static field B_0 of the shim-coil assisted magnet—in all three dimensions. All shim and gradient coils are planar-coil designed and fabricated by PCB to reduce the occupied gap inside the magnet. Current injections in these 8 pairs of coils are all independently controlled by microprocessors.

The permanent magnet, the RF coil, the 5 pairs of shim coils, the 3 pairs of gradient coils, and the electronics including the RF IC and microprocessors altogether weigh ~ 31 kg and occupy a volume of $40 \text{ cm} \times 25 \text{ cm} \times 25 \text{ cm}$.

1) *Customized RF IC*: The IC, fabricated in a standard 180-nm process, integrates an RF receiver, an RF transmitter, and a programmable arbitrary pulse sequencer for hardware miniaturization [32]. The receiver, headed by a low-noise amplifier, amplifies the spin precession signal captured by the RF coil and features quadrature mixers to down-convert the amplified signal into the intermediate frequency (<10 kHz). After passing through low-pass filters, these processed analog signals are digitized by external analog-to-digital converters (ADCs) for storing the acquired data in the microcontroller (MCU).

The transmitter embodies a multi-phase generator and a power amplifier. A benchtop signal generator (AFG31102, Tektronix USA) provides an RF reference signal for the multi-phase generator to generate 32-phase RF signals for synthesizing different NMR/MRI sequences. Then, the selected RF signals with desired phases are delivered to the power amplifiers, which inject the RF current into the coil to generate the magnetic field and excite the nuclear spins for yielding the desired MRI signals.

The pulse sequencer is a crucial component in mastering the execution of the MRI experiment with different pulse sequences. It reads the digital codes that represent the pattern and characteristics of the pulse sequence from the MCU via a standard peripheral interface and stores them in the on-chip memory array (64 lines of 64-bit data). Each line of data embeds the pulse information such as enable/disable of the receiver/transmitter, duration, phase of RF excitation signals, etc. All of the digital codes are written to the memory array before the beginning of the experiment. The pulse sequencer executes these pre-defined commands to govern the entire operation.

2) *Gradient Coils and Related Electronics*: To spatially encode the protons over the field-of-view (FOV) for MRI image reconstruction with precise synchronization with the RF IC, we propose an auxiliary electronic system to operate the current flow through the gradient coils for generating the magnetic field gradients. The electronic system consists of an FPGA development board (DE10-nano, Terasic, Taiwan), 10-bit digital-to-analog converters (DACs) (LTC2634, Analog Devices, USA), and coil drivers. The FPGA captures the trigger signal from the IC and sends the preset digital codes to the DACs through a customized serial peripheral interface (SPI) according to the MRI sequence. The DACs convert the input codes to analog voltages and feed them to the coil drivers for driving the gradient coils with appropriate currents. The core of the coil driver contains two signal amplification stages [Fig. 2(a)]. The first stage, based on an operational amplifier (OPA2990, Texas Instruments, USA) in the inverting configuration, converts the DAC's output voltage to a bipolar voltage between ± 5 V. The second stage, based on a high-current operational amplifier (OPA548, Texas Instruments, USA) in the inverting configuration, drives the required currents to the coils. The later operational amplifier is governed by an enable signal to ensure a complete cut-off when no current is required to drive the coil. We can express the

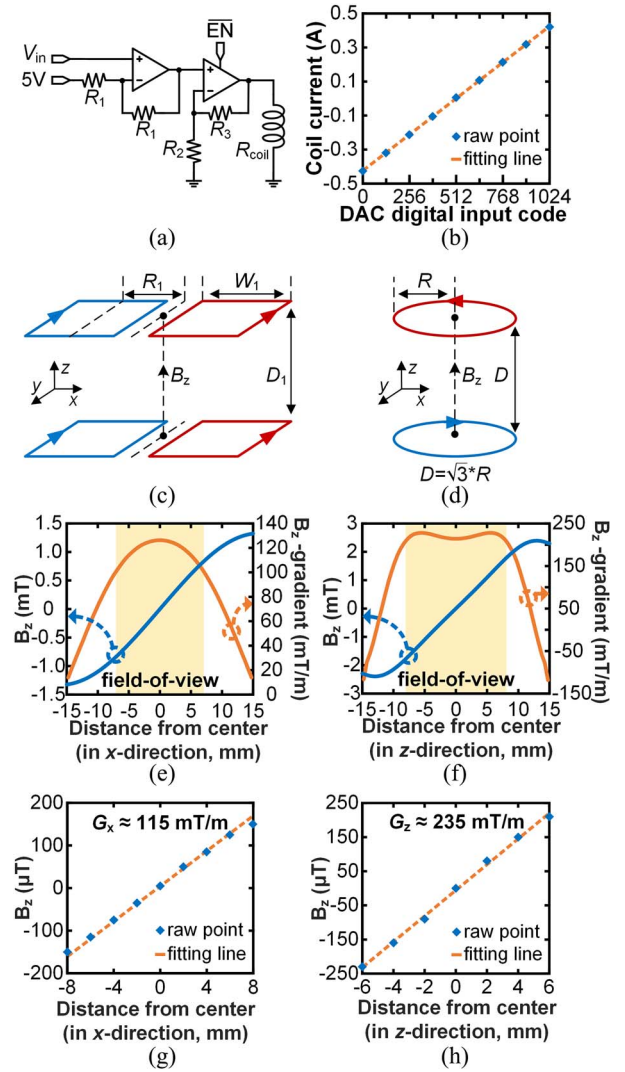


Fig. 2. (a) The schematic of the coil driver. It contains two amplification stages to convert the input voltage to the bipolar output coil current. (b) The current flows through the gradient coil in the x -direction versus the digital input code generated from the FPGA. (c) The structure of the x -direction gradient coil. (d) The structure of the z -direction gradient Maxwell coil. (e) The simulation results of the magnetic field and gradient strength in the z -direction along the x -axis. (f) The simulation results of the magnetic field and gradient strength in the z -direction along the z -axis. (g) The measurement results of the magnetic field in the z -direction along the x -axis by injecting a 0.16-A current into the coil and the calculated gradient strength. (h) The measurement results of the magnetic field in the z -direction along the z -axis and the calculated gradient strength.

current flowing through the gradient coil (I_{coil}) as

$$I_{\text{coil}} = \frac{(2V_{\text{in}} - 5) \left(1 + \frac{R_3}{R_2}\right)}{R_{\text{coil}}}, \quad (1)$$

where V_{in} is the output from the DAC. Fig. 2(b) shows the relationship between the digital codes and the corresponding measured current through the x -direction gradient coil (Power supply: 13 V, $R_{\text{coil}} = 29 \Omega$, $R_3/R_2 = 1.5$). The differential nonlinearity (DNL) and integral nonlinearity (INL) of the currents flowing through the gradient coils are $+0.27/-0.37$ and $+0.28/-0.25$ least significant bit (LSB, $\sim 817 \mu\text{A}$), respectively.

The measured rise and fall times (from 10% to 90% of the transition) of the current pulse is 1.2 μ s.

The x -direction gradient coil consists of four rectangular planar coils [Fig. 2(c)]. Two coils with opposite current directions are placed on the top plane, each with a width of W_1 (21.4 mm) and a separation of $2R_1$ (32.8 mm, in the x -direction) between the center of the coils. Two coils with the same configuration are placed on the bottom plane, where the separation between the top and bottom planes is D_1 (27.6 mm). These four coils combined generate a magnetic field gradient along the x -direction near the center. We verified the magnetic field gradient generated by this configuration and optimized its linearity by changing the mentioned parameters using the finite-element analysis tool. The simulated gradient at the center of the structure is 126 mT/m and drops by 20% at 7.5 mm from the center [Fig. 2(e)]. We measured the magnetic field generated by the gradient coils using a digital Teslameter (DTM-151, Group3, New Zealand). The measured gradient is 115 mT/m in the x -direction [Fig. 2(g)], which is consistent with the simulation results. We set the available field-of-view in the x -direction as 15 mm. The y -direction gradient coil has the exact geometry, except it is rotated by 90° around the z -axis to generate the gradient in the y -direction. Hence, the FOV on the xy -plane is 15 mm \times 15 mm.

For generating the z -direction magnetic field gradient, we adopted a Maxwell coil which consists of two circular coils with opposite current directions placed on two PCB planes [Fig. 2(d)]. We also optimized the geometric parameters for the multi-turn coil using the finite-element analysis tool. The simulated gradient strength in the z -direction is 215 mT/m at the center and drops by 15% at 8 mm from there [Fig. 2(f)]. The measured gradient along the z -direction is 235 mT/m [Fig. 2(h)]. The targeted resolution of the image should be smaller than the thickness of the biofilm/bacteria colony for effectively probing the T_2 of the protons at that location. Based on the observed thickness of the biofilms in the pipe from our experiments, the thickness will reach 400 μ m after a few days of cultures. Hence, we target a pixel resolution at the scale of 0.1 mm. Then, we designed the gradient coil drivers and their maximum currents according to the required resolution. As an illustration, by applying a current of 0.388 A into the frequency-encoding gradient coil (x -direction) and utilizing a 50-step phase encoding with 0.04-A step-current in the phase-encoding gradient coil (y -direction), we achieved an image resolution of 0.20×0.15 mm² for the T2WIs in the xy -plane.

3) *Shim Coils*: Achieving a homogeneous static magnetic field is vital for obtaining high-quality MRI images. We applied active shimming with shim coils to homogenize the magnetic field around the FOV to avoid image distortion attributable to the magnetic field inhomogeneity. In our system, we have 5 pairs of shim coils to correct different orders of the magnetic field. Three are linear magnetic-field shim coils to generate the gradient along the x -, y -, and z -directions, respectively, which are designed similarly to the gradient coils described above. These coils feature less turn but wider trace width than gradient coils, allowing for long-time and large current injection during shim operation. The last two pairs of shim coils are used for

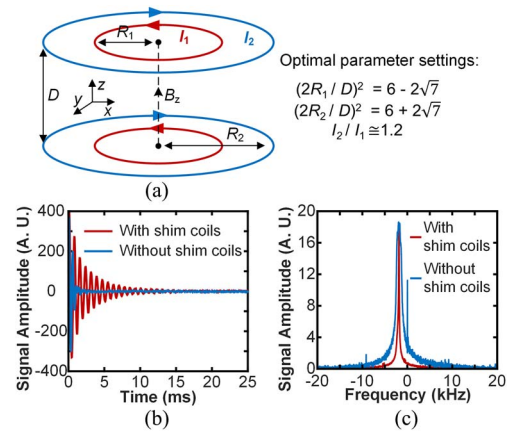


Fig. 3. (a) The structure of the shim coil for producing a quadratic shim field $B_z \propto (2z^2 - x^2 - y^2)$. (b) The comparison of the ¹H FID signals from water with and without shimming. (c) The frequency spectrum of the obtained FID signal in (b). By applying shimming, the FWHM of the spectrum improves from 1,400 Hz to 208.4 Hz (88.9 to 13.2 ppm at 0.37T).

correcting the quadratic inhomogeneity ($2z^2 - x^2 - y^2$) of the main magnetic field [45] [Fig. 3(a)].

The shim coils are enabled during the image acquisition phase to correct the field inhomogeneity. The MCU controls their magnitudes to obtain the optimum results with the corresponding DAC and coil drivers. We evaluate the shim performance by monitoring the free induction decay signal from a 0.5-ml centrifuge tube (Safe-Lock tube, Eppendorf, Germany) filled with water. Without shimming, the ¹H free-induction decay (FID) signal after fast Fourier transform (FFT) possesses a linewidth of 1,400 Hz (full-width at half-maximum, FWHM), equivalent to 88.7 ppm at 0.37 T. After applying shimming from five groups of shim coils, the FWHM of the FID signal improves to 208.4 Hz, or 13.2 ppm at 0.37T [Fig. 3(b) and 3(c)].

4) *RF Coil*: The RF coil is a 7-turn solenoid coil (length: 7 mm, diameter: 9.4 mm) wound with enamel copper wire (diameter: 1 mm). The measured inductance is 393 nH, with a quality factor of 78 (at 15.7 MHz). This RF coil is fastened on a 3D-printed holder to stabilize the coil's geometry.

B. Bacterial Culture Preparation

Escherichia coli (*E. coli*) K-12 strain MG1655 was selected as the sample for the MRI monitoring experiments. Before every MRI experiment, *E. coli* was incubated in the Luria-Bertani (LB) broth (Cat No. 12780052, Thermo Fisher, CA) at 37°C for 18 hours. Subsequently, the *E. Coli* solution was collected and diluted in the LB broth to achieve the desired bacterial concentration, which is determined from the optical density (OD) measurements (at 600 nm) using a microplate photometer (Multiskan FC, Thermo Fisher, CA). The *E. Coli* dilution with an OD value ranging from 0.6 to 0.7 absorbance units (A.U.) was chosen as the initial bacterial concentration for the later experiments, as this range indicates an optimal growth state for bacteria [46].

For the *in-situ* monitoring experiment, 20 μ L of the diluted *E. Coli* sample was added into a centrifuge tube containing 400 μ L of LB broth for further MRI detection.

To investigate the growth status of *E. Coli* under different conditions, we applied additional pretreatment procedures to the samples. Initially, three groups of diluted *E. Coli* samples (20 μL each) were collected and placed in separate centrifuge tubes. Then, one tube was subjected to ultraviolet (UV) light exposure for 4 hours to sterilize bacteria within the tube, which served as the control group. At the same time, the second and third tubes were cultured at room temperature (22°C) and 37°C inside the incubator for 4 hours, respectively. Subsequently, 400 μL of LB broth was added to each tube to provide the necessary nutrients. The first tube was exposed to the UV light for sterilization for 4 hours every day to inhibit bacteria growth and maintained at room temperature for the remaining time of the experiment.

C. Magnetic Field Fluctuation Calibration

To accelerate the MRI image acquisition, we use a single sequence of RF excitation pulses (turbo spin echo sequence with a turbo factor of 50; Fig. 4(a), top three rows), where the time to echo (T_E) can be adjusted, to obtain the NMR signal for constructing a T2WI (Fig. 4(a), bottom row). While a single scan—*i.e.*, one-time application of the pulse sequence—would be sufficient to create a T2WI in the absence of noise, in practice, we repeat the scan 192 times for signal averaging to improve the signal-to-noise ratio and thus the image quality, because the NMR signal from a single scan is weak due to the low static magnetic field ($B_0 \sim 0.37$ T) of the permanent magnet.

During the repeated scans, the B_0 field drifts due to the fluctuation of ambient temperature (temperature coefficient: $\sim 2,300$ ppm/K) [47], thus causing the base NMR frequency f_L to drift. Such f_L drift would blur the MRI image. There are various hardware and software techniques to circumvent such frequency drift [48], [49], [50].

Herein, we utilize a navigator signal to calibrate the image artifact due to the magnetic field fluctuation from the permanent magnet. Compared with the existing approach of acquiring frequency information through separate FID signals [51], our method does not require adding auxiliary excitation sequences, thus preserving the overall time for the experiment. During the data acquisition, each scan starts with acquiring an FID signal before running the turbo spin echo sequence [Fig. 4(a)]. The FID signal, obtained in the absence of gradient field activation, reveals f_L at the beginning of each scan, within the accuracy of the inhomogeneity of the shim-coil-assisted permanent magnet. This scheme enables image calibration at the software domain without adding extra hardware or any prior knowledge. During a multi-scan (N) MRI experiment, we can notate the magnet's field drift over time as

$$B(t) = B_0 + \Delta B(t), \quad (2)$$

where B_0 is the nominal magnetic field and $\Delta B(t)$ is the time-varying component due to deviation in temperature. Then, we can describe the f_L of the i -th ($i = 0, 1, \dots, N-1$) MRI scan as

$$\omega_i(t) = \gamma(B_0 + \Delta B_i(t)), \quad (3)$$

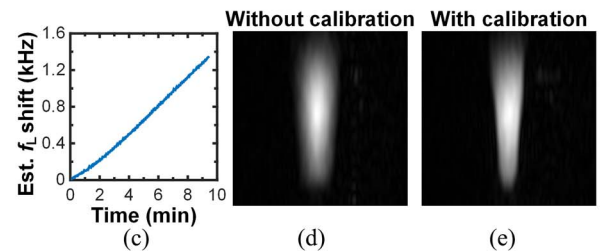
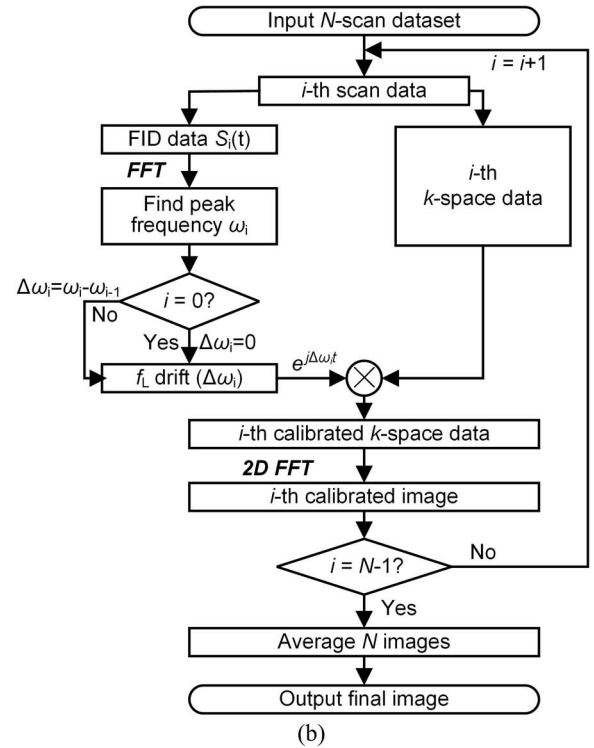
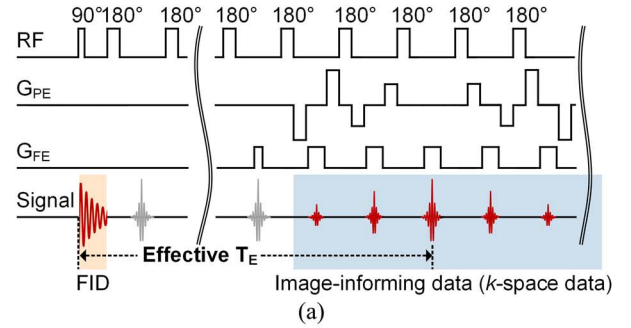


Fig. 4. (a) Turbo spin echo sequence for excitation (top three rows) and acquired NMR signal (bottom row) from which a T2WI is constructed. The sequence starts with an initial 90° excitation (top row) to obtain an FID (bottom row) to identify the f_L drift for calibration. G_{PE} and G_{FE} : applied gradient for phase encoding and frequency encoding. (b) Flow chart for magnetic field fluctuation calibration. (c) The measured f_L drift during 192 scans. (d) and (e) Acquired T2WIs of a water-filled centrifuge tube without and with f_L -drift calibration. $T_E = 106$ ms. Repetition time (T_R): 3 s.

where γ is the gyromagnetic ratio. We can rewrite this equation as

$$\omega_i(t) = \omega_0 + \Delta\omega_i(t), \quad (4)$$

where ω_0 is the nominal Larmor frequency and $\Delta\omega_i(t)$ is the drifting component. Since the temperature fluctuation is slow compared with the duration of a single scan (~ 500 ms), we omitted the effect caused by the f_L -drifting within an individual scan. If we

also neglect the imperfections in phase shift due to the off-resonance effect and nonuniform B_0 -weighting in the received signal, $\Delta\omega_i(t)$ evenly affects all spins in the detection volume. Consequently, we can treat $\Delta\omega_i(t)$ as a constant $\Delta\omega_i$ during a single scan. The FID signal captured from the i -th scan $[S_i(t)]$ can be simplified as

$$S_i(t) = A_i \int_{-\infty}^{+\infty} \rho_i(\omega) e^{-(t/T_2(\omega))} e^{-i(\omega+\Delta\omega_i)t} d\omega, \quad (t \geq 0) \quad (5)$$

$$S_i(t) = \frac{1}{2\pi} \int_{-\infty}^{+\infty} \widehat{\rho}_i(\omega) e^{-i(\omega+\Delta\omega_i)t} d\omega, \quad (t \geq 0) \quad (6)$$

where A_i is a complex amplitude representing the signal's strength and phase, $\rho(\omega)$ is the spectral density function characterizing the frequency distribution, $T_2(\omega)$ is the transverse relaxation time distribution, and ω is the precessing frequency in the rotating frame. The frequency spectrum $[\widehat{\rho}_i(\omega)]$ can be obtained by applying the fast Fourier transform (FFT) on the time-domain FID signal

$$\widehat{\rho}_i(\omega) = \int_0^\tau S_i(t) e^{i(\omega+\Delta\omega_i)t} dt. \quad (7)$$

To estimate the frequency drift of each scan, we set the frequency spectrum of the first MRI scan ($i = 0$) as the reference and designate the frequency of the maximum amplitude component as a hallmark ($\Delta\omega_0 = 0$). Then, we can use the offset value between the frequency of the maximum amplitude on the i -th scan's spectrum and the hallmark to estimate $\Delta\omega_i$.

We assume above that the frequency drift can be neglected when collecting MRI k -space data within a turbo spin-echo pulse sequence, owing to the slow temperature fluctuation during the short period. Hence, the entire collected k -space data in the i -th scan shares the same f_L -drift ($\Delta\omega_i$) calculated from the previous step. Then, the estimated $\Delta\omega_i$ from the FID of each scan can be used to shift the frequency of the k -space data to get the calibrated data of the corresponding scan as

$$S_{i,\text{cal}}(t) = e^{i\Delta\omega_i t} \cdot \iint \widehat{M}(x, y) e^{-i(\gamma(xG_x + yG_y) + \Delta\omega_i)t} dx dy, \quad (8)$$

where $\widehat{M}(x, y)$ is a factor proportional to the local proton density of the observed volume and G_x and G_y are the gradient strengths at point (x, y) . After applying a 2D FFT to (8), the resulting MRI image from the i -th scan has the same frequency baseline as the reference image ($i = 0$). Then, we perform averaging to all these calibrated images to enhance the signal-to-noise ratio. The entire calibration procedure is shown in Fig. 4(b).

D. Quantitative R_2 -Map Construction

Typical proton-density-based MRI is unsuitable for probing the biofilms or bacterial aggregations in a wet environment due to the lack of contrast in the density of ^1H nuclei between the biomass and the surrounding environment. Yet, studies have shown that the microbial cells and the biofilm matrix restrict the motion of water molecules in the vicinity, while the motion of bulk water molecules is unrestricted [52]. Additionally, the biofilm matrix could accumulate minerals from the growth medium,

leading to interactions between free metal ions and the matrix. Collectively, they result in the shortening of T_2 -relaxation and a decrease in the amplitude of the MRI signal [53]. Moreover, the changes in the composition and pH of the culture medium, caused by metabolic processes during bacterial growth, can also affect the apparent T_2 [20]. These factors provide the necessary signal contrast in T_2 between bacterial sites and the bulk environment, making T_2 -weighted MRI effective for visualizing bacterial growth and biofilm formation.

We construct R_2 maps ($R_2 = 1/T_2$) to quantitatively calculate the apparent T_2 distribution of the acquired images with different average T_E values, allowing for direct visualization of T_2 contrast. Specifically, we obtain the intensity of each pixel in the R_2 map by fitting the T_E of the T2WIs and their corresponding intensities (S) of the pixel via a mono-exponential decay function with a variable offset, as formulated by [44], [54]:

$$S(T_E) = A \cdot e^{(-T_E \cdot R_2)} + C. \quad (9)$$

Here, A is the projected intensity in the particular pixel at the beginning and C is a constant representing the system and sample noise. We generated the R_2 maps of the object by using the T2WIs acquired with seven different T_E evenly distributed between 161 and 785 ms for fitting the exponential function. Furthermore, if the pixels with intensities in the T2WI of $T_E = 161$ ms are lower than a threshold value (i.e., the region outside the tube area), we set their values in the R_2 map to zero to eliminate unnecessary disturbance from those areas and reduce the processing time.

III. RESULTS AND DISCUSSION

A. Verification of Magnetic Field Fluctuation Calibration

Fig. 4(c) shows the measured f_L drift while imaging a water-filled centrifuge tube consisting of 192 scans. Without calibration, the image is blurred and cannot portray the edge of the tube due to the drift of tube location on the image [Fig. 4(d)]. With the proposed calibration to track the f_L and re-center the frequency, the MRI image [Fig. 4(e)] can reconstruct the image details, manifesting the calibration scheme's appositeness. Note that these images are along the yz -plane (refer to Fig. 1 for the coordinate system we use) with no slice selection, i.e., an intensity at a given pixel at (y, z) in the yz -image integrates all the signal along the x -axis for the given (y, z) .

B. In Situ Monitoring of Bacterial Growth Over Time

It is crucial to ascertain that the magnetic field and MRI pulse have minimal effect on bacterial growth to utilize the miniaturized MRI system as an *in-situ* monitoring device. Hence, we conducted an experiment where the *E. Coli* was incubated under three different conditions to monitor their growth status using the spectrophotometer to measure the OD value of the sample. In the beginning, we injected the same concentration of *E. Coli* into seven centrifuge tubes, each containing 400 μL of LB broth. Of these seven tubes, three tubes were incubated outside the magnet and without RF magnetic fields acting as the control group, while the remaining four were incubated inside the

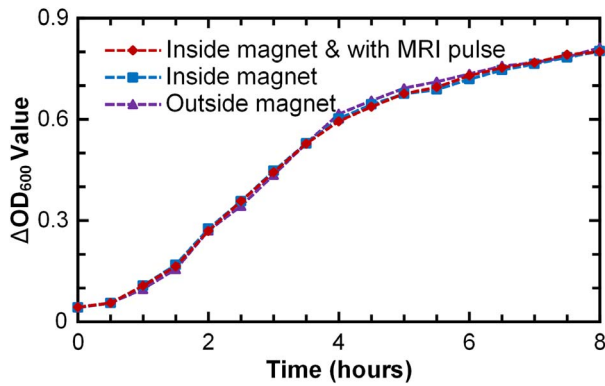


Fig. 5. The obtained OD value from the sample containing *E. Coli* and the culture media versus incubation time outside and inside the magnet, plus one with the MRI pulse sequences identical to the one applied in the actual imaging protocols (all at 37°C). No noticeable differences are observed in the growth speed or stages among the conditions.

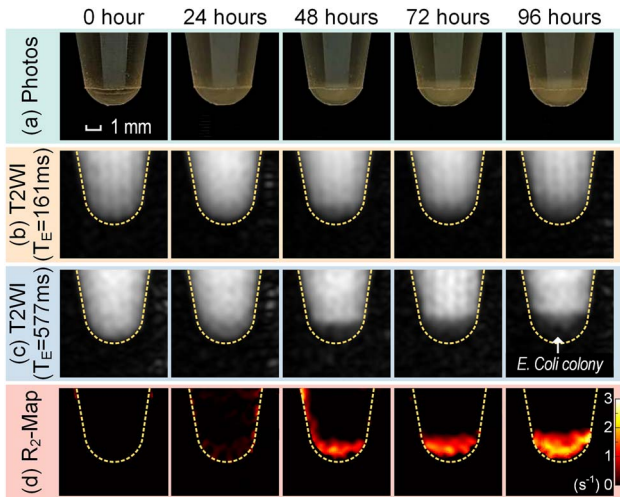


Fig. 6. (a) Photographs of a tube with cultured bacteria. (b) and (c) T2WIs of the sample with T_E of 161 and 577 ms after averaging 192 calibrated scan results. T_R : 5 s. (d) R_2 maps obtained from T2WIs with different T_E values.

magnet, where one of them was subjected to the MRI sequence (T_E : 577 ms; T_R : 5 s; number of averaging: 192). We set the temperature to 37°C for all tubes. As shown in Fig. 5, the OD values of all samples exhibit three growth stages (lag, exponential, and stationary) similar to the typical growth curve during an 8-hour interval. More importantly, no significant differences were observed in the growth speed or stages among different conditions (inside or outside the magnet, or with MRI sequence), thereby verifying that neither the static nor RF magnetic field affects bacterial growth.

For bacterial imaging on our miniaturized MRI platform, we culture *E. Coli* seeds in a centrifuge tube containing LB broth and monitor their growth for 96 hours (Fig. 6). Camera images [Fig. 6(a)] show that bacteria settle at the bottom of the tube due to gravity in the beginning and form an increasingly thicker layer over time with their growth. T2WIs—along the yz -plane with no slice section—acquired by our MRI system with sufficiently long T_E values show the formation of the colonies. According to

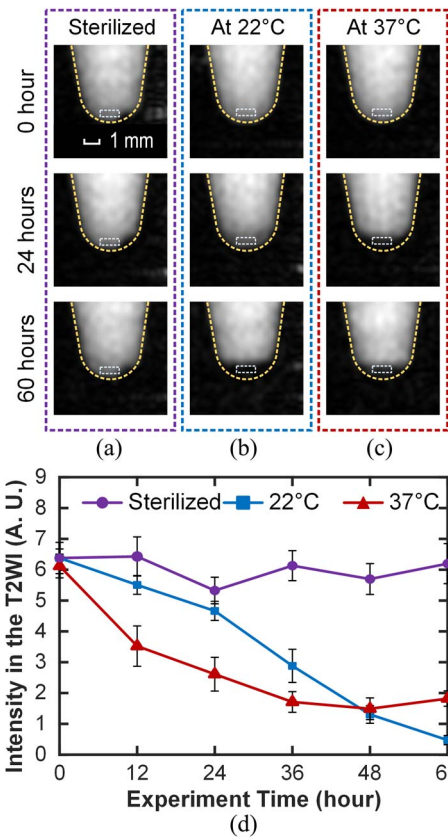


Fig. 7. (a)–(c) Obtained T2WIs (after averaging 192 calibrated scan results) from three different bacteria samples, one in a tube sterilized by ultraviolet (UV) light, and the other two in unsterilized tubes at 22°C and 37°C. T_E : 577 ms. T_R : 5 s. (d) The T2WI intensity averaged across the squared marked region for each sample vs. time.

the T_2 -weighted theories, the contrast between the two objectives features different T_2 can be enhanced when increasing the effective T_E value of the RF pulse sequence [Fig. 4(a)]. Concretely, for a short enough T_E of 161 ms [Fig. 6(b)], T2WI intensities remain similar across the entire tube regardless of time elapse, but for a long enough T_E of 577 ms [Fig. 6(c)], with time elapse T2WI intensities become increasingly weaker (darker) towards the bottom part of the tube where *E. Coli* colony is formed, because the higher bacterial density, the shorter T_2 .

For every 24 hours, we acquire T2WIs with seven different T_E values and generate a spatial map of R_2 values (Fig. 6). As seen in Fig. 6(d), at the beginning, the T_2 distribution is uniform across the tube. As time elapses, T_2 values at the bottom of the tube gradually decrease and the region of such decreased T_2 expands. This attests to bacterial growth upward from the bottom of the tube. While both camera images [Fig. 6(a)] and MRI results (either T2WIs of Fig. 6(c) or the R_2 map of Fig. 6(d)) can track bacterial growth, the MRI method has the advantage of being able to track bacteria growth inside an opaque tube.

To further substantiate the finding that MRI results reflect bacterial growth, we culture *E. Coli* with the same amount of inoculation in three centrifuge tubes, which are subjected to different treatments: one tube is sterilized, and the other two tubes,

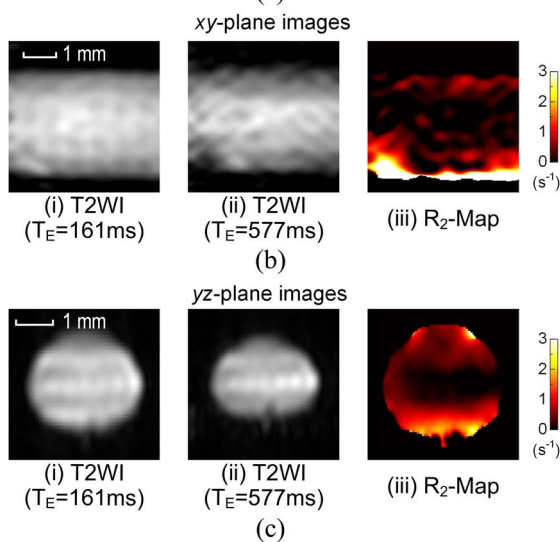
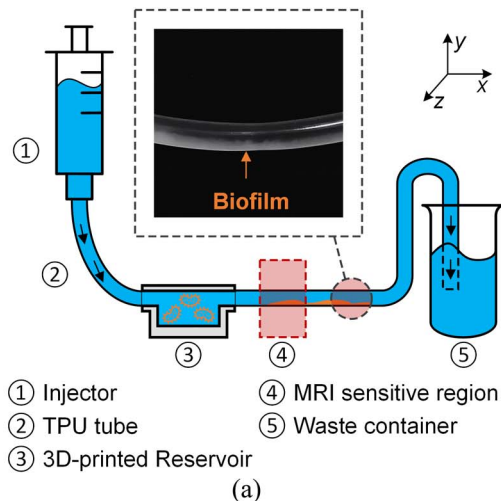


Fig. 8. (a) Setup to monitor a biofilm inside a thermoplastic elastomer pipe (TPU, inner diameter: 3 mm). To provide adequate nutrition for bacterial growth, we inject 10 mL of broth into the pipe at a speed of around 2 mL/min every 12 hours using an injector. Bacteria are initially inoculated inside a 3D-printed reservoir and then flow through the tube to aggregate and form biofilm on the tube's inner surface caused by the injection operation. A 3D-printed reservoir is used not only for the initial inoculation of bacteria but also for slowing down the flow rate of broth injection and increasing the probability of bacteria attaching to the inner surface. Transparent TPU is chosen so that it is easy to verify the correctness of MRI imaging results and whether there is a biofilm. The inserted camera image illustrates biofilm formation inside the tube. (b) xy T2WIs (each obtained after averaging 192 calibrated scan results) and xy R_2 map. (c) yz T2WIs (each obtained after averaging 192 calibrated scan results) and yz R_2 map. $T_R = 5$ s. Each R_2 map in (b) and (c) is obtained from seven T2WIs with seven T_E values evenly distributed from 161 to 785 ms.

which are unsterilized, are kept at 22°C and 37°C. We obtain T2WIs—again along the yz -plane with no slice section—of these three tubes every 12 hours over 60 hours [Fig. 7(a)–7(c)]. For the sterilized tube where bacterial growth is inhibited, the T2WI intensities remain uniform and unaltered for 60 hours [Fig. 7(a)]. This serves as a foil to the case of Fig. 6(c)–6(d) and implies that the changes in T2WIs of Fig. 6 are associated with bacterial growth and aggregation rather than the sedimentation of initial inoculation volume. Meanwhile, for the unsterilized tubes kept at 22°C and 37°C, bacteria grow over time, as

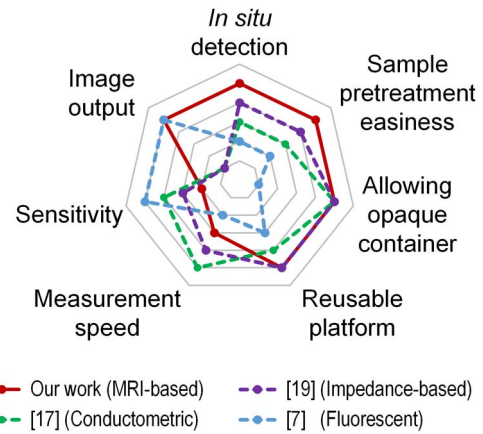


Fig. 9. A radar chart comparing the characteristics of bacterial monitoring utilizing different mechanisms.

confirmed by the eventual emergence of dark regions at the bottom of the T2WIs [Fig. 7(b)–7(c)]. Moreover, we track the T2WI intensities in the square-marked regions in three tubes [Fig. 7(a)–7(c)] as quantitative indicators of bacterial density and show the results in Fig. 7(d). As seen, the intensity exhibits, at least for the first 48 hours, a faster decay at 37°C than at 22°C, which agrees with the fact that *E. Coli* grows faster at 37°C than at room temperature [55]. The reversal of the signal intensity after 48 hours may be due to the promotion of expression of biofilm-dependent genes at low temperatures after bacteria changed from planktonic state to biofilm phase [56].

C. Biofilm Distribution Inside Tube Monitoring

To further demonstrate the capability of the MRI system to image bacterial development, such as biofilm formation inside the container, we utilize our MRI system to take images of a bacteria biofilm inside a thermoplastic elastomer pipe [Fig. 8(a)], where the inserted figure shows the camera image of biofilm in the inner wall of the pipe. This time, we take xy images with no slice selection [Fig. 8(b)] and yz images with no slice selection [Fig. 8(c)], after a 96-hour culture (the coordinate system of Fig. 8 is consistent with that of Fig. 1). Both xy and yz T2WIs with a long enough T_E of 577 ms show biofilm formation in parts of the inner wall of the pipe, and so do xy and yz R_2 -maps [Fig. 8(b) and 8(c)]. These results demonstrate the ability of our small MRI platform to provide 3D perspectives of bacteria biofilm. We also conducted a similar experiment where the medium inside the tube flowed at a rate of 10 $\mu\text{L}/\text{min}$. The resulting images show similar patterns of biofilm and bacteria colony formations, indicating the system's feasibility to monitor bacterial growth amid liquid flow inside the tube.

IV. CONCLUSION AND DISCUSSION

In conclusion, we have demonstrated an application of a miniaturized MRI system for *in situ*, non-invasive monitoring of bacterial growth and colony formation, representing an

advancement in the field of microbiology. MRI images taken by the small platform inform quantifiable spatial distributions of bacteria density. Due to it eliminating the need for sample preparation, immobilized biocomponent, or the opening of sample-containing tubes or pipes, the MRI-based technique might serve as a complementary alternative to optical and electrochemical methods for on-site tracking of bacterial growth and imaging bacterial distribution (Fig. 9). Our study demonstrated the platform's functionality, providing evidence of its potential in real-time, non-invasive monitoring of bacterial populations.

The proposed platform opens up new avenues for studying bacterial dynamics *in situ* and in real-time, both in the laboratory and in the field, and provides an alternative to monitoring bacterial populations, leading to advancements in areas such as disease diagnostics, antimicrobial susceptibility testing, environmental microbiology, and biotechnological processes. Moreover, the platform could serve as a foundation for developing similar portable MRI technologies for monitoring other biological entities, such as viruses, fungi, or biological cells. This would expand the scope of portable MRI technology, advancing it beyond bacteria monitoring and bringing it to the forefront of various scientific and clinical domains.

REFERENCES

- [1] R. L. Nichols, "Postoperative infections in the age of drug-resistant gram-positive bacteria," *Amer. J. Med.*, vol. 104, no. 5, pp. 11S–16S, May 1998.
- [2] M. S. Olson, R. M. Ford, J. A. Smith, and E. J. Fernandez, "Quantification of bacterial chemotaxis in porous media using magnetic resonance imaging," *Environ. Sci. Technol.*, vol. 38, no. 14, pp. 3864–3870, Jul. 2004.
- [3] J. Wingender and H.-C. Flemming, "Contamination potential of drinking water distribution network biofilms," *Water Sci. Technol.*, vol. 49, nos. 11–12, pp. 277–286, Jun. 2004.
- [4] B. E. Logan, "Exoelectrogenic bacteria that power microbial fuel cells," *Nature Rev. Microbiol.*, vol. 7, no. 5, pp. 375–381, May 2009.
- [5] R. Funari and A. Q. Shen, "Detection and characterization of bacterial biofilms and biofilm-based sensors," *ACS Sens.*, vol. 7, no. 2, pp. 347–357, Feb. 2022.
- [6] H. Chuang, P. Macuch, and M. B. Tabacco, "Optical sensors for detection of bacteria. I. General concepts and initial development," *Anal. Chem.*, vol. 73, no. 3, pp. 462–466, Feb. 2001.
- [7] Z. Zhou, Y. Zhang, M. Guo, K. Huang, and W. Xu, "Ultrasensitive magnetic DNAzyme-copper nanoclusters fluorescent biosensor with triple amplification for the visual detection of *E. coli* O157:H7," *Biosens. Bioelectron.*, vol. 167, Nov. 2020, Art. no. 112475.
- [8] F. C. Dudak and İ. H. Boyacı, "Rapid and label-free bacteria detection by surface plasmon resonance (SPR) biosensors," *Biotechnol. J.*, vol. 4, no. 7, pp. 1003–1011, Jul. 2009.
- [9] K. Syal et al., "Antimicrobial susceptibility test with plasmonic imaging and tracking of single bacterial motions on nanometer scale," *ACS Nano*, vol. 10, no. 1, pp. 845–852, Jan. 2016.
- [10] A. Roda et al., "Progress in chemical luminescence-based biosensors: A critical review," *Biosens. Bioelectron.*, vol. 76, pp. 164–179, Feb. 2016.
- [11] J. de D. Habimana, J. Ji, and X. Sun, "Minireview: Trends in optical-based biosensors for point-of-care bacterial pathogen detection for food safety and clinical diagnostics," *Anal. Lett.*, vol. 51, no. 18, pp. 2933–2966, Dec. 2018.
- [12] S.-N. Hosseini, P. S. Das, V. K. Lazarjan, G. Gagnon-Turcotte, K. Bouzid, and B. Gosselin, "Recent advances in CMOS electrochemical biosensor design for microbial monitoring: Review and design methodology," *IEEE Trans. Biomed. Circuits Syst.*, vol. 17, no. 2, pp. 202–228, Apr. 2023.
- [13] X. Muñoz-Berbel, N. Vigués, A. T. A. Jenkins, J. Mas, and F. J. Muñoz, "Impedimetric approach for quantifying low bacteria concentrations based on the changes produced in the electrode–solution interface during the pre-attachment stage," *Biosens. Bioelectron.*, vol. 23, no. 10, pp. 1540–1546, May 2008.
- [14] E. Ghafar-Zadeh, M. Sawan, V. P. Chodavarapu, and T. Hosseini-Nia, "Bacteria growth monitoring through a differential CMOS capacitive sensor," *IEEE Trans. Biomed. Circuits Syst.*, vol. 4, no. 4, pp. 232–238, Aug. 2010.
- [15] N. Jo et al., "Aptamer-functionalized capacitance sensors for real-time monitoring of bacterial growth and antibiotic susceptibility," *Biosens. Bioelectron.*, vol. 102, pp. 164–170, Apr. 2018.
- [16] L. Li, X. Liu, W. A. Qureshi, and A. J. Mason, "CMOS amperometric instrumentation and packaging for biosensor array applications," *IEEE Trans. Biomed. Circuits Syst.*, vol. 5, no. 5, pp. 439–448, Oct. 2011.
- [17] L. Yao et al., "CMOS conductometric system for growth monitoring and sensing of bacteria," *IEEE Trans. Biomed. Circuits Syst.*, vol. 5, no. 3, pp. 223–230, Jun. 2011.
- [18] M. S. Mannoor et al., "Graphene-based wireless bacteria detection on tooth enamel," *Nature Commun.*, vol. 3, no. 1, Mar. 2012, Art. no. 763.
- [19] X. Zhang et al., "Online monitoring of bacterial growth with an electrical sensor," *Anal. Chem.*, vol. 90, no. 10, pp. 6006–6011, May 2018.
- [20] V. Hoerr et al., "Assessment of inhibitory potency of antibiotics by MRI: Apparent t_2 as a marker of cell growth," *Magn. Reson. Mater. Phys., Biol. Med.*, vol. 19, no. 5, pp. 247–255, Nov. 2006.
- [21] S. L. Codd et al., "NMR relaxation measurements of biofouling in model and geological porous media," *Org. Geochem.*, vol. 42, no. 8, pp. 965–971, Sep. 2011.
- [22] S. J. Vogt, A. B. Sanderlin, J. D. Seymour, and S. L. Codd, "Permeability of a growing biofilm in a porous media fluid flow analyzed by magnetic resonance displacement-relaxation correlations," *Biotechnol. Bioeng.*, vol. 110, no. 5, pp. 1366–1375, May 2013.
- [23] C. M. Kirkland et al., "Biofilm detection in a model well-bore environment using low-field NMR," *Groundwater Monit. Remediation*, vol. 35, no. 4, pp. 36–44, Nov. 2015.
- [24] Y. Zhang, Y. Lin, X. Lv, A. Xu, C. Feng, and J. Lin, "Low-field nuclear magnetic resonance characteristics of biofilm development process," *Microorganisms*, vol. 9, no. 12, Dec. 2021, Art. no. 2466.
- [25] A. B. Sanderlin, S. J. Vogt, E. Grunewald, B. A. Bergin, and S. L. Codd, "Biofilm detection in natural unconsolidated porous media using a low-field magnetic resonance system," *Environ. Sci. Technol.*, vol. 47, no. 2, pp. 987–992, Jan. 2013.
- [26] C. M. Kirkland et al., "In situ detection of subsurface biofilm using low-field NMR: A field study," *Environ. Sci. Technol.*, vol. 49, no. 18, pp. 11045–11052, Sep. 2015.
- [27] J. D. Seymour, J. P. Gage, S. L. Codd, and R. Gerlach, "Magnetic resonance microscopy of biofouling induced scale dependent transport in porous media," *Adv. Water Resour.*, vol. 30, no. 6, pp. 1408–1420, Jun. 2007.
- [28] L. Caizán-Juanarena et al., "3D biofilm visualization and quantification on granular bioanodes with magnetic resonance imaging," *Water Res.*, vol. 167, Dec. 2019, Art. no. 115059.
- [29] P. P. Stang, S. M. Conolly, J. M. Santos, J. M. Pauly, and G. C. Scott, "Medusa: A scalable MR console using USB," *IEEE Trans. Med. Imag.*, vol. 31, no. 2, pp. 370–379, Feb. 2012.
- [30] S. Fan, Q. Zhou, K.-M. Lei, P.-I. Mak, and R. P. Martins, "Miniaturization of a nuclear magnetic resonance system: Architecture and design considerations of transceiver integrated circuits," *IEEE Trans. Circuits Syst. I, Reg. Papers*, vol. 69, no. 8, pp. 3049–3060, Aug. 2022.
- [31] N. Sun, T.-J. Yoon, H. Lee, W. Andress, R. Weissleder, and D. Ham, "Palm NMR and 1-chip NMR," *IEEE J. Solid-State Circuits*, vol. 46, no. 1, pp. 342–352, Jan. 2011.
- [32] D. Ha, J. Paulsen, N. Sun, Y.-Q. Song, and D. Ham, "Scalable NMR spectroscopy with semiconductor chips," *Proc. Nat. Acad. Sci.*, vol. 111, no. 33, pp. 11955–11960, Aug. 2014.
- [33] K.-M. Lei, P.-I. Mak, M.-K. Law, and R. P. Martins, "NMR–DMF: A modular nuclear magnetic resonance–digital microfluidics system for biological assays," *Analyst*, vol. 139, no. 23, pp. 6204–6213, 2014.
- [34] F. Dreyer, Q. Yang, B. Alnajjar, D. Krüger, B. Blümich, and J. Anders, "A portable chip-based NMR relaxometry system with arbitrary phase

- control for point-of-care blood analysis,” *IEEE Trans. Biomed. Circuits Syst.*, vol. 17, no. 4, pp. 831–842, Aug. 2023.
- [35] J. Reber et al., “An in-bore receiver for magnetic resonance imaging,” *IEEE Trans. Med. Imag.*, vol. 39, no. 4, pp. 997–1007, Apr. 2020.
- [36] S. Fan, Q. Zhou, K.-M. Lei, P.-I. Mak, and R. P. Martins, “A miniaturized 3-D-MRI scanner featuring an HV-SOI ASIC and achieving a $10 \times 8 \times 8$ mm³ field of view,” *IEEE J. Solid-State Circuits*, vol. 58, no. 7, pp. 2028–2039, Jul. 2023.
- [37] D. Krüger et al., “A portable CMOS-based spin resonance system for high-resolution spectroscopy and imaging,” *IEEE J. Solid-State Circuits*, vol. 58, no. 7, pp. 1838–1849, Jul. 2023.
- [38] E. Danieli, J. Perlo, B. Blümich, and F. Casanova, “Small magnets for portable NMR spectrometers,” *Angew. Chem. Int. Ed.*, vol. 49, no. 24, pp. 4133–4135, Jun. 2010.
- [39] A. Bashyam et al., “A portable single-sided magnetic-resonance sensor for the grading of liver steatosis and fibrosis,” *Nature Biomed. Eng.*, vol. 5, no. 3, pp. 240–251, Nov. 2020.
- [40] T. O’Reilly, W. M. Teeuwisse, D. de Gans, K. Koolstra, and A. G. Webb, “In vivo 3D brain and extremity MRI at 50 mT using a permanent magnet Halbach array,” *Magn. Reson. Med.*, vol. 85, no. 1, pp. 495–505, 2021.
- [41] Y. Liu et al., “A low-cost and shielding-free ultra-low-field brain MRI scanner,” *Nature Commun.*, vol. 12, no. 1, 2021, Art. no. 7238.
- [42] B. Sporrer et al., “A fully integrated dual-channel on-coil CMOS receiver for array coils in 1.5–10.5 T MRI,” *IEEE Trans. Biomed. Circuits Syst.*, vol. 11, no. 6, pp. 1245–1255, Dec. 2017.
- [43] D. G. Thomas et al., “Single-sided magnet system for quantitative MR relaxometry and preclinical in-vivo monitoring,” *IEEE Trans. Biomed. Eng.*, vol. 70, no. 2, pp. 671–680, Feb. 2023.
- [44] K.-M. Lei et al., “Portable NMR with parallelism,” *Anal. Chem.*, vol. 92, no. 2, pp. 2112–2120, Jan. 2020.
- [45] W. A. Anderson, “Electrical current shims for correcting magnetic fields,” *Rev. Sci. Instrum.*, vol. 32, no. 3, pp. 241–250, Mar. 1961.
- [46] A. Kobayashi, H. Hirakawa, T. Hirata, K. Nishino, and A. Yamaguchi, “Growth phase-dependent expression of drug exporters *Escherichia coli* and its contribution to drug tolerance,” *J. Bacteriol.*, vol. 188, no. 16, pp. 5693–5703, Aug. 2006.
- [47] K. M. Lei, P.-I. Mak, M.-K. Law, and R. P. Martins, “A thermal-insensitive all-electronic modular μ NMR relaxometer with a 2D digital microfluidic chip for sample management,” in *Proc. 19th Int. Conf. Miniaturized Syst. Chem. Life Sci (MicroTAS)*, Gyeongju, Korea, 2015, p. 302.
- [48] D. Tamada and K. Kose, “Two-dimensional compressed sensing using the cross-sampling approach for low-field MRI systems,” *IEEE Trans. Med. Imag.*, vol. 33, no. 9, pp. 1905–1912, Sep. 2014.
- [49] C. Z. Cooley et al., “Two-dimensional imaging in a lightweight portable MRI scanner without gradient coils,” *Magn. Reson. Med.*, vol. 73, no. 2, pp. 872–883, Feb. 2015.
- [50] J. Meineke and T. Nielsen, “Data consistency-driven determination of B₀-fluctuations in gradient-echo MRI,” *Magn. Reson. Med.*, vol. 81, no. 5, pp. 3046–3055, 2019.
- [51] “*ParaVision 360 user manual*,” Bruker Corporation, Billerica, MA, USA, Version 001, Jul. 26, 2018. [Online]. Available: <https://www.bruker.com/es/products-and-solutions/preclinical-imaging/paravision-360.html>
- [52] T. R. Neu, B. Manz, F. Volke, J. J. Dynes, A. P. Hitchcock, and J. R. Lawrence, “Advanced imaging techniques for assessment of structure, composition and function in biofilm systems,” *FEMS Microbiol. Ecol.*, vol. 72, no. 1, pp. 1–21, Apr. 2010.
- [53] J. Bartacek, F. J. Vergeldt, J. Maca, E. Gerkema, H. Van As, and P. N. L. Lens, “Iron, cobalt, and gadolinium transport in methanogenic granules measured by 3D magnetic resonance imaging,” *Frontiers Environ. Sci.*, vol. 4, pp. 1–8, Mar. 2016, Art. no. 13.
- [54] J. C. Wood et al., “MRI R₂ and R₂* mapping accurately estimates hepatic iron concentration in transfusion-dependent thalassemia and sickle cell disease patients,” *Blood*, vol. 106, no. 4, pp. 1460–1465, Aug. 2005.
- [55] S. Y. Lee, “High cell-density culture of *Escherichia coli*,” *Trends Biotechnol.*, vol. 14, no. 3, pp. 98–105, Mar. 1996.
- [56] C. A. White-Ziegler, S. Um, N. M. Pérez, A. L. Berns, A. J. Malhowski, and S. Young, “Low temperature (23 °C) increases expression of biofilm-, cold-shock- and RpoS-dependent genes in *Escherichia coli* K-12,” *Microbiology*, vol. 154, no. 1, pp. 148–166, Jan. 2008.



Qi Zhou (Graduate Student Member, IEEE) received the B.Sc. degree in instrument science and engineering from Southeast University, Nanjing, China, in 2017, and the M.Sc. degree in electronics and communications engineering from Sun Yat-sen University, Guangzhou, China, in 2019. He is currently working toward the Ph.D. degree in electrical and computer engineering (ECE) with the University of Macau, Macau. His current research interests include portable nuclear magnetic resonance (NMR), magnetic resonance imaging (MRI) systems, and related applications.



Shuhao Fan (Graduate Student Member, IEEE) received the B.Sc. degree in electronic and information engineering from Northeast Forestry University, Harbin, China, in 2016, and the M.Sc. degree in IC design engineering from The Hong Kong University of Science and Technology (HKUST), Hong Kong, in 2017. She is currently working toward the Ph.D. degree in electrical and computer engineering (ECE) with the University of Macau, Macau. Her research interests include portable nuclear magnetic resonance (NMR) systems and miniaturized magnetic resonance imaging (MRI) platforms.



Ka-Meng Lei (Senior Member, IEEE) received the B.Sc. degree in electrical and electronic engineering (EEE) and the Ph.D. degree in electrical and computer engineering (ECE) from the University of Macau, Macau, in 2012 and 2016, respectively. He has been serving as an Assistant Professor with the University of Macau since 2019. From 2017 to 2019, he was a Postdoctoral Fellow with Harvard University, where he was involved in developing the high-resolution portable nuclear magnetic resonance (NMR) spectrometer. He has published 40+ refereed papers. He has co-authored one book *Handheld Total Chemical and Biological Analysis Systems: Bridging NMR, Digital Microfluidics, and Semiconductors* (Springer 2018), and two book chapter *Micro-NMR on CMOS for Biomolecular Sensing* (Springer 2018) and *Ultra-Low-Voltage Clock References* (Springer 2023). His current research interests include ultralow voltage analog circuit techniques, sensors and analog front-end interfaces, and high-resolution portable NMR platforms. Since 2021, he has been a TPC Member of the IEEE International Conference on Integrated Circuits, Technologies and Applications (ICTA). He is a Committee Member for the IEEE SSCS Young Professionals, coordinating the Webinars for Young Excellence Program. He was a (co-)recipient of the Chipidea Microelectronics Prize 2017 (Postgraduate), the Best Paper Award in ASQED 2013, the Distinguished Design Award from the IEEE Asian Solid-State Circuits Conference (A-SSCC) 2015, the Silkroad Award from the ISSCC 2016, the FDCT Macao Science and Technology Award for Postgraduates in 2016, the 2016 Young Researcher Award from the Instituto Internacional de Macau, the IEEE SSCS Predoctoral Achievement Award in 2017, and the Best Poster Award from the Workshop on IC Advances in China (ICAC) 2023. He was on the Organizing Committee of the IEEE A-SSCC 2019. He currently serves as an Associate Editor of IEEE TRANSACTIONS ON BIOMEDICAL CIRCUITS AND SYSTEMS and IEEE OPEN JOURNAL OF CIRCUITS AND SYSTEMS.

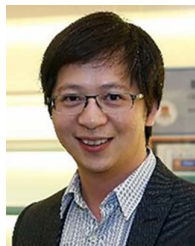


Donhee Ham (Fellow, IEEE) is currently a Gordon McKay Professor of applied physics and electrical engineering with Harvard University, Cambridge, MA, USA, where he has been a Faculty Member since 2002. He is a Samsung Fellow. His current research interests include semiconductor-bio interfaces for neuroscience, machine intelligence, and biological data archiving; scalable nuclear magnetic resonance (NMR); integrated circuits; neuromorphic and in-sensor computing; and beyond CMOS electronics.



Rui P. Martins (Life Fellow, IEEE), received the Ph.D. degree in electrical engineering and computers from the Department of Electrical and Computer Engineering, Instituto Superior Técnico, University of Lisbon, Portugal, in 1992. He has been with the Department of Electrical and Computer Engineering, Instituto Superior Técnico, University of Lisbon, since October 1980. From 1992, he has been on leave from the University of Lisbon and with the Department of Electrical and Computer Engineering, Faculty of Science and Technology, University of

Macau, Macao, China, where he has been a Chair-Professor since August 2013. His research interests include analog and mixed-signal VLSI design. He has authored or co-authored 900+ publications, including 10 books, 12 book chapters, 50 patents, 300+ papers in scientific journals, and 400+ in conference proceedings. He was the Founding Director of the State Key Laboratory of Analog and Mixed-Signal VLSI, between 2011 and 2022, and he is currently the Director of the Institute of Microelectronics, with the University of Macau, Macao, China. He received the Author Recognition Award at the 70 years of ISSCC, in 2023, as a Top Contributor with more than 50 papers, and three Medals from Macao Government, in 1999, 2001, and 2021. Since July 2010, he has been an Academician with the Lisbon Academy of Sciences, Portugal.



Pui-In Mak (Fellow, IEEE) received the Ph.D. degree from the University of Macau (UM), Macao, China, in 2006. He is currently a Professor with the UM Faculty of Science and Technology—ECE Department, the Director with the State Key Laboratory of Analog and Mixed-Signal VLSI, and the Deputy Director (Research) with the Institute of Microelectronics. His research interests include analog and radio-frequency (RF) circuits and systems for wireless and multidisciplinary innovations. His involvements with IEEE are the Member of Board-

of-Governors of IEEE Circuits and Systems Society (2009–2011); a Senior Editor of IEEE JOURNAL ON EMERGING AND SELECTED TOPICS IN CIRCUITS AND SYSTEMS (2014–2015); and the Editorial Board Member of IEEE PRESS (2014–2016); and an Associate Editor of IEEE TRANSACTIONS ON CIRCUITS AND SYSTEMS II: REGULAR PAPERS (2010–2013), IEEE TRANSACTIONS ON CIRCUITS AND SYSTEMS I: REGULAR PAPERS (2010–2011 and 2014–2015), IEEE SOLID-STATE CIRCUITS LETTERS (2017), and IEEE JOURNAL OF SOLID-STATE CIRCUITS (2018). He is/was a TPC Member of A-SSCC (2013–2016 and 2019), the TPC Vice co-chair of ASP-DAC (2016), ESSCIRC (2016–2017), and ISSCC (2017–2019). He is/was the Distinguished Lecturer of IEEE Circuits and Systems Society (2014–2015) and IEEE Solid-State Circuits Society (2017–2018). He was the Chairman of the Distinguished Lecturer Program of IEEE Circuits and Systems Society (2018–2019). He has (co-)received the DAC/ISSCC Student Paper Award 2005, the CASS Outstanding Young Author Award 2010; the National Scientific and Technological Progress Award 2011; the Best Associate Editor of IEEE TRANSACTIONS ON CIRCUITS AND SYSTEMS II: EXPRESS BRIEF 2012–2013, the A-SSCC Distinguished Design Award 2015, the ISSCC Silkroad Award 2016, and the Xplorer Prize 2022. In 2005, he was decorated with the Honorary Title of Value for scientific merits by the Macau Government. He has been inducted as an Overseas Expert of the Chinese Academy of Sciences since 2018, a fellow of the U.K. Institution of Engineering and Technology (IET) for contributions to engineering research, education and services since 2018, and a fellow of the IEEE for contributions to radio-frequency and analog circuits since 2019, and a fellow of the U.K. Royal Society of Chemistry since 2020.